J Appl Electrochem (2008) 38:131–149
DOI 10.1007/s10800-007-9411-4

ORIGINAL PAPER

Modeling a perforated bipole trickle bed electrochemical reactor for the generation of alkaline peroxide

Neeraj Gupta · Colin W. Oloman

Received: 9 April 2007 / Revised: 13 July 2007 / Accepted: 30 August 2007 / Published online: 2 October 2007

Abstract This paper describes the modeling of a novel perforated bipole electrochemical reactor with trickle-bed cathodes employed in the electrosynthesis of alkaline peroxide solutions. The model engages an electronic analogue of the 3D electrode/bipoles to solve the coupled material, energy and voltage (charge) balances that estimate the potential, current density, composition, pressure and temperature profiles through the reactor. The predictions of this model are compared to the performance of a bench scale experimental reactor operating at superficial current densities up to 5 kA m^{-2}. With eddy diffusion through the diaphragm as the single adjustable parameter the model shows good agreement with peroxide current efficiency but underestimates the electrochemical specific energy consumption by about 2 kWh/kg H_2O_2 at 5 kAm^{-2}.

Keywords Electroreduction · Oxygen · Peroxide · Electrochemical · Electrosynthesis · 3D electrodes · Perforated bipole · Trickle-bed · Graphite felt · Modeling

Symbols

a_a	Tafel parameter for reaction (4) on the anode (V)
a_{c1}	Tafel parameter for reaction (1) on the cathode (V)
a_{c2}	Tafel parameter for reaction (2) on the cathode (V)
b_a	Tafel slope for reaction (4) on the anode (V $decade^{-1}$)
b_{c1}	Tafel slope for reaction (1) on the cathode (V $decade^{-1}$)
b_{c2}	Tafel slope for reaction (2) on the cathode (V $decade^{-1}$)
C	Reactant concentration (kmol m^{-3})
C_{aOH^-}	Concentration of hydroxyl ion on the anode side (kmol m^{-3})
C.B.	Fraction current bypass in the reactor (dimensionless)
C.E.	Current efficiency (dimensionless)
$C_{electrolyte\ (j)}$	Concentration of electrolyte j (kmol m^{-3})
$C_{electrolyte,O_2}$	O_2 concentration in electrolyte (kmol m^{-3})
$C_{HO_2^-}$	Concentration of per hydroxyl ion (kmol m^{-3})
C_{H_2O,O_2}	O_2 concentration in water (kmol m^{-3})
C_{NaOH,O_2}	O_2 concentration in NaOH (kmol m^{-3})
C_{Na^+}	Concentration of sodium ion (kmol m^{-3})
C_{O_2}	Concentration of oxygen (kmol m^{-3})
C_{OH^-}	Concentration of hydroxyl ion (kmol m^{-3})
c_l	Liquid heat capacity (kJ $kg^{-1}K^{-1}$)
c_g	Gas heat capacity (kJ $kg^{-1}K^{-1}$)
D	Dispersion coefficient (m^2 s^{-1})
$D_{HO_2^-}$	Diffusivity of perhydroxyl ion (m^2 s^{-1})
D_{O_2}	Diffusivity of oxygen (m^2 s^{-1})
D_{OH^-}	Diffusivity of perhydroxyl ion (m^2 s^{-1})
D_{Na^+}	Diffusivity of sodium ion (m^2 s^{-1})
$D^0_{HO_2^-}$	Diffusivity of perhydroxyl ion at infinite dilution (m^2 s^{-1})
$D^0_{O_2}$	Diffusivity of oxygen at infinite dilution (m^2s^{-1})
$D^0_{OH^-}$	Diffusivity of hydroxyl ion at infinite dilution (m^2s^{-1})
$D^0_{Na^+}$	Diffusivity of sodium ion at infinite dilution (m^2s^{-1})

N. Gupta (✉) · C. W. Oloman
Department of Chemical & Biological Engineering, University of British Columbia, Vancouver, BC, Canada V6T1Z4
e-mail: neeraj.gupta@momentive.com

$D_{dHO_2^-}$	Effective diffusivity of perhydroxyl ion in the diaphragm (m^2s^{-1})
D_{dOH^-}	Effective diffusivity of hydroxyl ion in the diaphragm (m^2s^{-1})
D_{ed}	Eddy diffusivity of hydroxyl ion (convection) (m^2s^{-1})
D_L	Diffusivity of liquid (m^2s^{-1})
d_f	Fibre diameter (m)
E_{a1}	Activation energy for reaction (1) on carbon (kJ $kmol^{-1}$)
E_{a2}	Activation energy for reaction (2) on carbon (kJ $kmol^{-1}$)
$E_{H_2O_2}$	Activation energy for H_2O_2 decomposition reaction (3) (J mol^{-1})
F	Faraday's constant (96486) (kC $kmol^{-1}$)
G	Gas load (kg $m^{-2}s^{-1}$)
g	Gas (oxygen) flow rate (kg s^{-1})
H	Henry's constant for oxygen in NaOH (kmol kg^{-1} $m^{-2}s^2$)
H_O	Henry's constant for oxygen in H_2O (kmol kg^{-1} $m^{-2}s^2$)
h_G	Sechenov parameter (dimensionless)
h_i	Sechenov parameter (dimensionless)
h_l	Liquid hold up (dimensionless)
$I_{reactor}$	Total current fed to the reactor (A)
I_1	Current transferred due to electrochemical reactions (A)
I_2	Current bypass through the reactor (A)
$i_{1HO_2^-}$	Superficial current density for reaction (4) on the anode in cell 1 (A m^{-2})
$i_{2HO_2^-}$	Superficial current density for reaction (4) on the anode in cell 2 (A m^{-2})
i_{1OH^-}	Superficial current density for reaction (5) on the anode in cell 1 (A m^{-2})
i_{2OH^-}	Superficial current density for reaction (5) on the anode in cell 2 (A m^{-2})
$i_{HO_2^-}$	Superficial current density for reaction (4) on the anode (A m^{-2})
i_{OH^-}	Superficial current density for reaction (5) on the anode (A m^{-2})
j	Current density (A m^{-2})
$j_{cathode}$	Total real current density for reaction (1) & (2) on the cathode (A m^{-2})
$j_{HO_2^-}$	Real current density for reaction (1) on the graphite felt cathode (A m^{-2})
j_{OH^-}	Real current density for reaction (2) on the graphite felt cathode (A m^{-2})
j_{lim1}	Mass transfer limited real current density for oxygen transfer (A m^{-2})
j_{lim2}	Mass transfer limited real current density for perhydroxyl ion transfer (A m^{-2})
j(1)	Total superficial current density on the anode for (4) & (5) (A m^{-2})
j(k)	Real current density for (1) on cell1: where k = 2, 4,....(n–1)/2 (A m^{-2})
	Real current density for (2) on cell1: where k = 3, 5,....(n–1)/2 + 1 (A m^{-2})
	Real current density for (1) on cell 2: where k = (n–1)/2 + 2, (n–1)/2 + 2 ....(n–1) (A m^{-2})
	Real current density for (2) on cell 2: where k = (n–1)/2 + 3, (n–1)/2 + 5 ....n n = 4m+1, where m is an integer (A m^{-2})
$j_{1HO_2^-}$	Real current density for reaction (1) on the graphite felt of cell 1 (A m^{-2})
$j_{2HO_2^-}$	Real current density for reaction (1) on the graphite felt of cell 2 (A m^{-2})
j_{1OH^-}	Real current density for reaction (2) on the graphite felt of cell 1 (A m^{-2})
j_{2OH^-}	Real current density for reaction (2) on the graphite felt of cell 2 (A m^{-2})
j_{01}	exchange current density for reaction (1) on graphite (A m^{-2})
j_{02}	exchange current density for reaction (2) on graphite (A m^{-2})
j_{0a}	exchange current density for reaction (4) on nickel (A m^{-2})
$K_{s,j}$	Sechenov constant (l mol^{-1})
$k_{contact}$	Contact area conductivity of grafoil and graphite felt (S m^{-2})
k_{apl}	Electrolyte (solution) conductivity (S m^{-1})
k_{apb}	Effective electrolyte conductivity in the graphite felt (S m^{-1})
k_{apd}	Effective electrolyte conductivity in the diaphragm (S m^{-1})
k_{aps}	Effective electrode conductivity (graphite felt) (S m^{-1})
$k_{grafoil}$	Conductivity of grafoil (S m^{-1})
k_{perf}	Perforation electrolyte conductivity (S m^{-1})
k_{H_2O}	Mass transfer coefficient for water transfer (m s^{-1})
$k_{HO_2^-}$	Overall mass transfer coefficient for per hydroxyl ion (m s^{-1})
k_m	Mass transfer coefficient (m s^{-1})
k_O	Overall mass transfer coefficient for O_2 transfer (m s^{-1})
k_1	Electrochemical rate constant for reaction (1) (m s^{-1})
k_2	Electrochemical rate constant for reaction (2) (m s^{-1})
k^0	Electrochemical rate constant at a defined temperature (m s^{-1})
k_1^0	Electrochemical rate constant for reaction (1) at 288 K (m s^{-1})

k_2^0	Electrochemical rate constant for reaction (2) at 288 K (m s^{-1})
k_a^o	Standard rate constant (anodic) (m s^{-1})
k_c^o	Standard rate constant (cathodic) (m s^{-1})
l_e	Length of reactor (m)
lin	Number of length increments of the reactor (dimensionless)
liq	Liquid flow rate (electrolyte) (kg s^{-1})
ln	Log to the base e (2.7123 approx.)
log	Log to the base 10
M_{O_2}	Molecular weight of oxygen (0.032) (kg mol^{-1})
$MW_{product}$	Molecular weight of product (kg $kmol^{-1}$)
NHE	Normal hydrogen electrode potential (298 K and 101 kPa abs.): defined as 0 V (V)
n	Number of equations to be solved for the two cell reactor where n = 4m+1, where m is an integer
n_{cell}	Number of cells in the reactor
n_i	Number of ions in the electrolyte (dimensionless)
n_o	Number of electrons exchanged in the reaction (dimensionless)
perf	Fraction perforation area in the bipolar electrode (dimensionless)
P	Reactor pressure (kPa)
P_{H_2O}	Vapour pressure of water (kPa)
P_{O_2}	Partial pressure of O_2 (kPa)
R	Gas constant, (8.314) (kJ $kmol^{-1}K^{-1}$)
S.E.	Specific energy (electrochemical) (kWh/kg)
s	Specific surface area of the bed (m^{-1})
T	Temperature (K)
t_b	Cathode matrix (graphite felt) thickness after compression (m)
t_d	Diaphragm thickness (m)
t_o	Cathode matrix (graphite felt) thickness before compression (m)
t_{perf}	Thickness of perforation (m)
u	Electrolyte velocity in direction of flux (m s^{-1})
U_G	Superficial gas velocity (m s^{-1})
U_L	Superficial liquid velocity (m s^{-1})
V_c	Voltage per cell (V)
V_{cf}	Electrolyte potential at the face of the cathode bed (V)
$V_{contact1}$	Contact resistance between grafoil and graphite felt at bipolar electrode (V)
$V_{contact2}$	Contact resistance between grafoil and graphite felt at end cathode (V)
V_d	Diaphragm potential drop (V)
V_r	Reactor voltage (V)
V_{ra}	Equilibrium potential for reaction (4) on anode (V)
V_c^R	Equilibrium potential (measured w.r.t. SHE) of cathode (V)
V_c^o	Standard equilibrium potential (measured w.r.t. SHE) of cathode at unit activity of reactants and products (V)
V_{rc}	Equilibrium potential for a cathodic reaction (V)
V_{rc1}	Equilibrium potential for reaction (1) (V)
V_{rc2}	Equilibrium potential for reaction (2) (V)
w	Width of the reactor (m)
x	Distance (m)
$z_{HO_2^-}$	Charge on perhydroxyl ion (1) (dimensionless)
z_{Na^+}	Charge on sodium ion (1) (dimensionless)
z_{OH^-}	Charge on hydroxyl ion (1) (dimensionless)

Superscripts

new	Value at exit in Figure 12

Greek Symbols

α	Charge transfer coefficient (dimensionless)
α_1	Electrochemical charge transfer coefficient for reaction (1) (dimensionless)
α_2	Electrochemical charge transfer coefficient for reaction (2) (dimensionless)
ε_b	Graphite felt porosity after compression (dimensionless)
ε_d	Diaphragm porosity (dimensionless)
η_a	Anodic overpotential (V)
η_{aOH^-}	Overpotential for reaction (4) on anode (V)
η_c	Cathodic overpotential (V)
η_{c1}	Overpotential for reaction (1) on the cathode (V)
η_{c2}	Overpotential for reaction (2) on the cathode (V)
μ_G	Gas viscosity (kg $m^{-1}s^{-1}$)
μ_L	Liquid viscosity (kg $m^{-1}s^{-1}$)
τ	Residence time in the reactor (s)
ρ_L	Liquid (electrolyte) density (kg m^{-3})
ρ_G	Gas (oxygen) density (kg m^{-3})
σ	Standard deviation (dimensionless)
ϕ	potential (V)
ϕ_s	Electrode potential (V)
ϕ_b	Electrolyte potential (V)
ΔHevap	Heat of vaporization of water (kJ/mol)
∇P_{LG}	Two-phase pressure gradient (kg $m^{-2}s^{-2}$)
Δl	Length of the graphite felt fibre, (m)
ΔP_{LG}	Two-phase pressure drop (kg m^{-1} s^{-2})
Δz	Thickness of the cross-section in Figure 7 (m)
τ	is the residence time in the model (described above)

1 Introduction

Alkaline peroxide generation using a novel perforated bipole trickle bed electrochemical reactor has been described in our previous work [1, 2]. Each cell in the electrochemical reactor uses a flow-by electrode as shown in Fig. 1. Subsequently we presented experimental work [3] on scaling-up both one and two-cell reactors from a cathode size of 120 mm long (l_e) by 25 mm wide (w) by 3.2 mm thickness (t_b) (reactor-A) to 630 mm long by 40 mm wide by 3.2 mm thickness (reactor-B). In order to interpret the effect of scale-up and to design a practical multi-cell industrial reactor it is desirable to model the perforated bipole trickle bed electrochemical reactor for peroxide generation.

Earlier work on modeling a conventional single-cell trickle-bed reactor for peroxide generation has been done by Oloman [4], Spalek [5] and more recently by Sudoh et al. [6]. These models used approximations such as isothermal operation with the rate of peroxide generation under kinetic control [4] and neglected the 3D electrode potential gradient [5, 6]. A more comprehensive single-cell model for use in reactor scale-up is complicated by accounting for the electrode potential gradient in the mixed control regime (i.e. mass transport and kinetics are of the same order of magnitude) as well as pressure and temperature gradients and the effects of axial and transverse dispersion in the cathode. In the special case of a perforated bipole reactor the bipole perforations further complicate the modeling work, as they allow current to bypass each cell, causing loss in peroxide current efficiency. The intent of this paper is to describe a model for the perforated bipole electrochemical reactor and compare the modeling results with experimental data.

2 Experimental

The experimental set-up of the perforated bipole trickle bed electrochemical reactor-B and corresponding experimental results are as previously published [2, 3]. The experiments described below were carried out to provide further information on reaction kinetics and fluid dispersion necessary for the reactor model.

2.1 Reaction kinetics

The reactions taking place in the electrochemical reactor are summarized in Table 1. The intrinsic kinetic parameters of the reactions (1), (2) and (4) are taken from the literature (see Table 4), while reaction (3) is considered insignificant from previous experience showing negligible H_2 under similar process conditions.

The kinetics of the thermochemical peroxide decomposition reaction (6) were determined experimentally by measuring the rate of peroxide decomposition in 500 ml glass flasks at 41, 60 and 80 °C, in 2M aqueous NaOH with the electrolyte additives 0.002%$_w$ Makon NF-12 (wetting agent) and 0.1%$_w$ DTPA (chelating agent). The peroxide decomposition rates are shown in Fig. 2 and the corresponding first order rate constants at 41, 60 and 80 °C, are 8×10^{-6}, 6×10^{-5} and 7×10^{-4} s^{-1} respectively. The rate constants from Fig. 2 are plotted against the inverse of temperature in Fig. 3 to give the activation energy ($E_{H_2O_2}$) for peroxide decomposition as 1.02×10^5 J mol^{-1}. Erdey and Inczedy [7] have measured the activation energy for peroxide decomposition in alkaline solutions to be 8.4×10^4 J mol^{-1}, and Enestova et al. [8] found it to be 9.2×10^4 J mol^{-1}.

2.2 Dispersion

To measure the extent of axial dispersion in the perforated bipole electrochemical reactor, tracer tests were done on the reactor-B with a gasketed graphite felt cathode sandwiched between the two electrode plates as shown in Fig. 4. With the 6 mm thick graphite felt compressed to

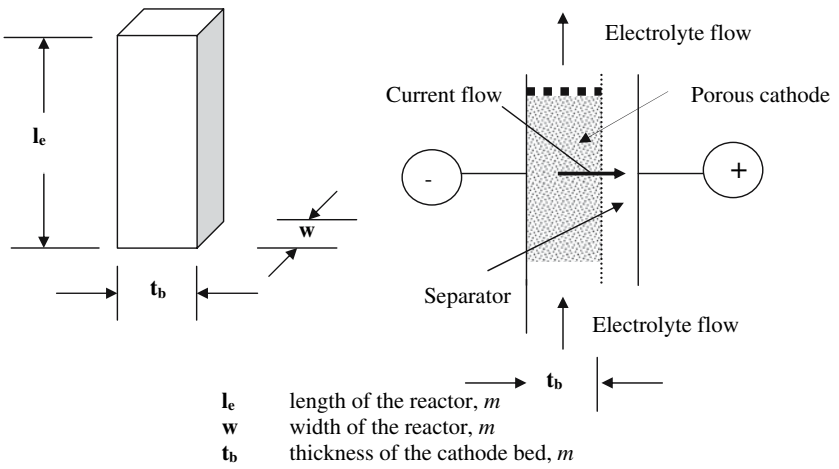

Fig. 1 Flow-by electrode

Table 1 Reactions in electro-synthesis of alkaline peroxide

Reaction	E_e° V vs. NHE at 298 K (pH = 14)	
Cathode		
$O_2 + H_2O + 2e^- \Rightarrow OH^- + HO_2^-$	–0.076	1
$HO_2^- + H_2O + 2e^- \Rightarrow 3OH^-$	+0.878	2
$2H_2O + 2e^- \Rightarrow H_2 + 2OH^-$	–0.830	3
Anode		
$O_2 + 2H_2O + 4e^- \Leftarrow 4OH^-$	+0.401	4
$O_2 + H_2O + 2e^- \Leftarrow OH^- + HO_2^-$	–0.076	5
Bulk		
$2HO_2^- \Rightarrow 2OH^- + O_2$	–	6

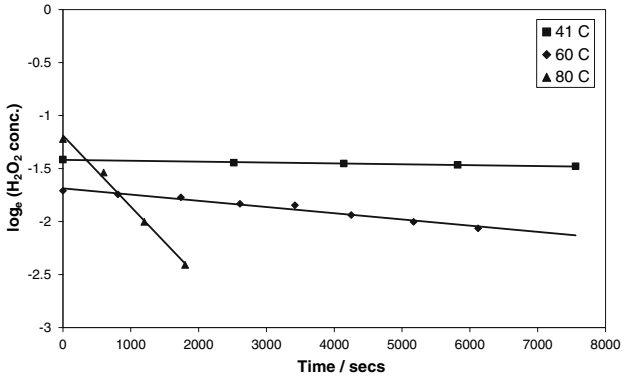

Fig. 2 Determination of rate constant for peroxide decomposition at different temperatures (41, 60 and 80 °C) and 2 M NaOH

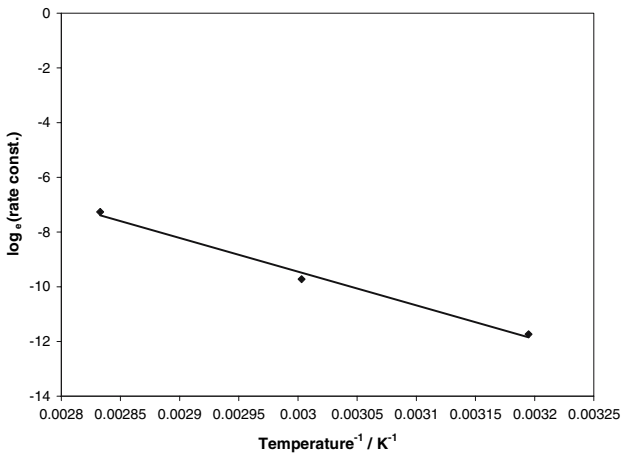

Fig. 3 Determination of activation energy for peroxide decomposition

3.2 mm water and O_2 were fed from the bottom of the reactor and withdrawn from the top. A small amount of tracer (0.5 ml of 0.5%$_w$ NaCl solution) was injected at the inlet of the reactor using a syringe in pulse mode (very short time span <1 s), the conductivity change was monitored with time at the reactor exit using a conductivity probe and the data (conductivity vs. time) recorded by computer. The water and O_2 flow rates correspond to the electrolyte and O_2 flow rates typically used in the electrochemical reactor for alkaline peroxide generation in the present work.

The conductivity versus time data was converted to a graph of relative concentration versus time, such as that shown in Fig. 5. To analyze the results of the tracer tests, equations describing the flow pattern (closed-closed boundary condition) based on Fig. 6 were used in the present work [9]. All symbols and units used here are as defined in the Nomenclature.

The variance for the dispersion graphs is given by the following equation:

$$\sigma^2/\tau^2 = 2(D/(U_L l_e)) - 2(D/(U_L l_e))^2(1 - \exp\{-(U_L l_e)/D\}) \quad (7)$$

The standard deviation (σ) is calculated as the deviation on the time axis from the mean, comprising 68% of the area under the curve or equivalently as the time width with 61% of the peak on the Gaussian curves (e.g. Fig. 5).

The average residence time τ in the reactor was obtained from:

$$\tau = \frac{\text{Reactor volume for water flow}}{\text{liquid flow rate}} = \frac{\varepsilon_b t_b w l_e h_l}{(\text{liq}/\rho_L)} \quad (8)$$

where the liquid hold-up in the reactor is given by [10]:

$$h_l = 1 - 0.907(\text{liq}/(t_b w))^{-0.362}(g/(t_b w))^{0.301} \quad (9)$$

Based on Eqs. 7–9 the liquid phase dispersion numbers ($D/U_L l_e$) calculated for the three fluid loads are given in Table 2. The dispersion numbers reported in Table 2 are for the liquid (water) flow and have been calculated by accounting for the liquid hold-up h_l in the reactor.

3 Modeling

3.1 Assumptions

(1) Convection through the diaphragm in the model is accounted for by the eddy diffusivity (D_{ed}) term. This term is added to the diffusive term to account for the total diffusive plus convective loss of peroxide through the diaphragm
(2) The conductivity of the electrolyte in the perforations is assumed to be independent of oxygen flow (i.e. the perforations are filled with electrolyte)
(3) The reactor operates in plug flow with:
- Zero axial dispersion of both phases (along the length (l_e) of reactor)

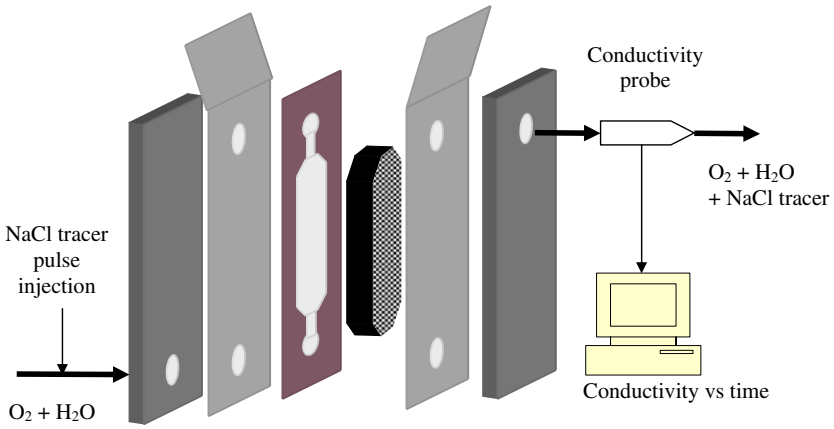

Fig. 4 Tracer test on reactor-B

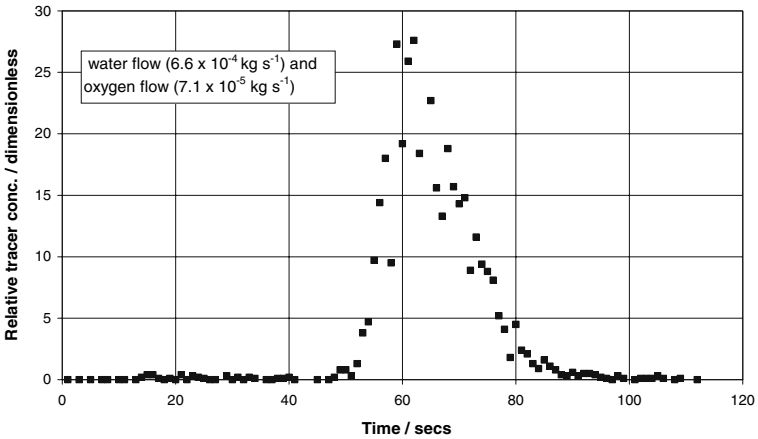

Fig. 5 Relative tracer concentration versus time for water flow (6.6×10^{-4} kg s^{-1}) and oxygen flow (7.1×10^{-5} kg s^{-1}) in reactor-B

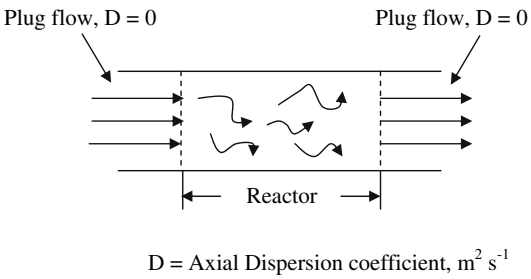

Fig. 6 Flow pattern for the peroxide reactor [9]

- Infinite lateral dispersion of both phases (through the thickness (t_b) of the 3D cathode)

The assumption of zero axial dispersion was based on the low liquid phase axial dispersion numbers of Table 2. The assumption of infinite transverse dispersion (i.e. perfect mixing across the cathode thickness) is somewhat problematic since it is based only on the visual observation of 2-phase (G/L) flow in a transparent version of reactor-B [3].

3.2 Two-cell bipolar reactor model

Figure 7 shows the conceptual two-cell reactor assembly used in the experimental work on the multi-cell system. It may be seen from Fig. 7 that O_2 gas and NaOH solution enter the reactor from the bottom and the product peroxide in alkaline solution exits the reactor at the top. Peroxide in the form of perhydroxyl ion, HO_2^- accumulates in the 3D cathode via reaction (1) minus reaction (2) and hydroxyl ions together with perhydroxyl are transferred through the diaphragm to undergo oxidation at the anode via reactions (4) and (5). The microporous separator suppresses the transport of perhydroxyl to the anode to an extent that depends on the concentrations and diffusivities of OH^- and HO_2^- and the relative magnitudes of convection versus diffusion plus migration in general flux equation.

In the two-cell reactor the central perforated Grafoil sheet is a bipolar electrode. It behaves as an anode on one side and a cathode on the other, but its performance in this respect is imperfect because electrolyte in the perforations provide an ionic current path between the two sides of the bipole. As shown in Fig. 8 this bypass current, "leaks" through the bipole without undergoing electrochemical (Faradaic) reactions and is therefore a source of loss in peroxide current efficiency. This loss in current efficiency may be calculated based on the illustration in Fig. 9.

The perforations normally experience 2-phase flow of gas and liquid. The relative amounts of gas and liquid in the perforations is difficult to calculate but perforations

Table 2 Dispersion number values

Water flow rate (liq: kg s^{-1})	O_2 flow rate (g: kg s^{-1})	Liquid hold up (h_l)	Standard deviation (σ: s)	Mean residence time (τ: s)	Dispersion number ($D/U_L\ l_e$)
6.6×10^{-4}	–	1	7	104	0.002
6.6×10^{-4}	4.3×10^{-5}	0.65	6	69	0.004
6.6×10^{-4}	7.1×10^{-5}	0.58	6	61	0.005

As the values of the dispersion numbers were between low (<0.002) and intermediate (<0.025) (Levenspiel, 3), zero axial dispersion was a reasonable assumption

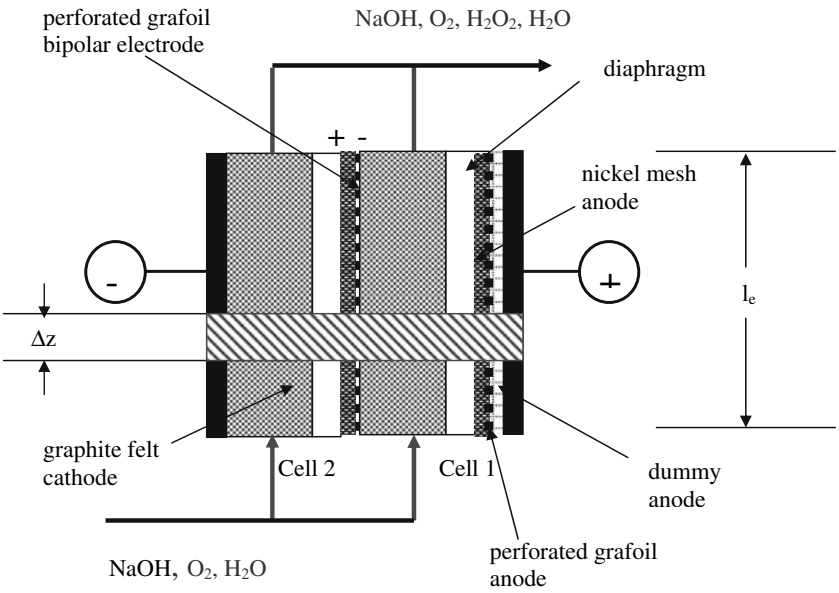

Fig. 7 Two-cell reactor model

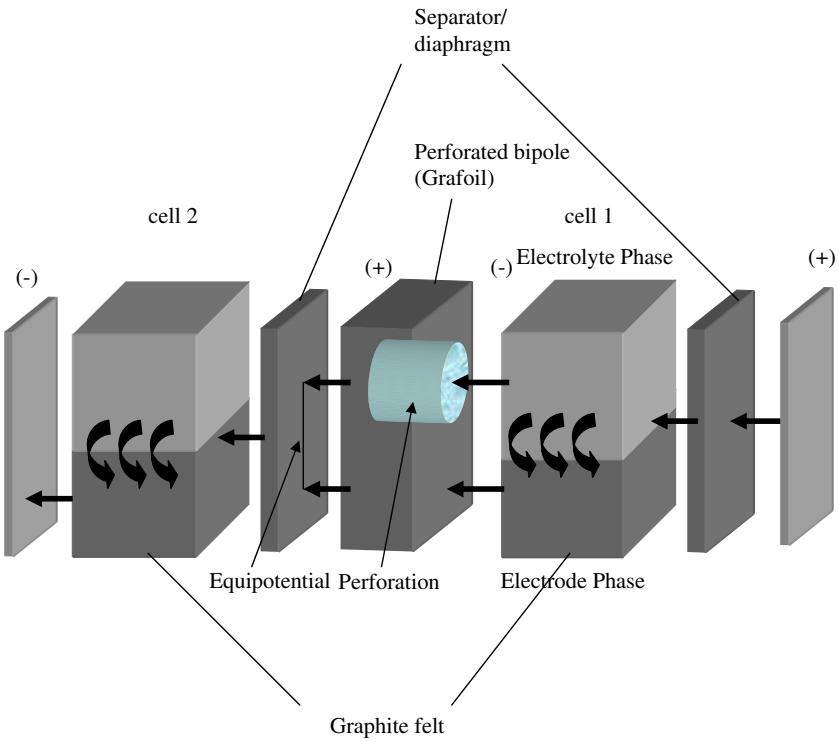

Fig. 8 Current bypass through a perforation assumes perforations filled fully with electrolyte (NaOH)

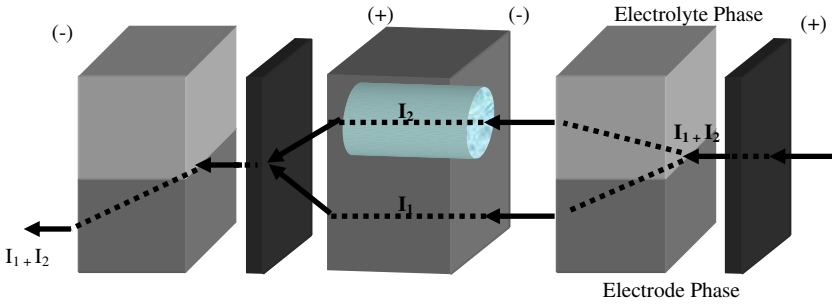

Fig. 9 Current bypass mechanism in a two-cell assembly

filled with liquid provide a sufficient and conservative guide for scaling-up the electrochemical reactor. Therefore, the perforations in the bipole electrodes are assumed completely filled with electrolyte (NaOH).

It may be observed from Fig. 9 that current $I_1 + I_2$ flows from the right through the diaphragm in the electrolyte phase. Of this total current ($I_1 + I_2$), current I_1 flows into the cathode (electrode phase). Current I_2 bypasses the electrode through the perforation. So the useful current for cell 1 is only I_1. However, for cell 2, all the current ($I_1 + I_2$) passes into the electrode phase before exiting the reactor. So current I_1 passes through the cathode beds of both the cells and participates in electrochemical reactions on the cathode bed, whereas current I_2 is transferred via electrochemical reactions (1), (2) and (3) in the cathode bed of cell 2 only. For this reason the current bypass may be derived from the following equations, in which all symbols and units are as defined in the Nomenclature.

The currents I_1 and I_2 are calculated based on their fractional area coverages. i.e. the current densities at the electrode and the perforation were multiplied by their respective fractional areas while solving the voltage balance equations.

Fractional current bypass for two cells in series

$$= \frac{I_2}{2(I_1 + I_2)} \tag{10}$$

Likewise:

Fractional current bypass for three cells in series

$$= \frac{2I_2}{3(I_1 + I_2)} \tag{11}$$

and

Fractional current bypass for n_{cell} cells in series

$$= \frac{(n_{cell} - 1)I_2}{(n_{cell})(I_1 + I_2)} \tag{12}$$

If n_{cell} is large (> 20) then

$$\text{Fractional current bypass} = \frac{I_2}{(I_1 + I_2)} \tag{13}$$

The bipolar reactor section shown in Fig. 10 is modeled based on a voltage balance. Conventionally the voltage balance is done by solving Poisson's equation

$$\nabla^2(\phi_s - \phi_b) = -s\left(\frac{1}{k_{aps}} + \frac{1}{k_{apb}}\right)j \tag{14}$$

Equation 14 in one space dimension translates into

$$\frac{d^2(\phi_s - \phi_b)}{dx^2} = s\left(\frac{1}{k_{aps}} + \frac{1}{k_{apb}}\right)j \tag{15}$$

where j is typically a non-linear function of (ϕ_s–ϕ_b).

Equation 14 is a non-linear partial differential equation and can be solved in one dimension by converting it to a non-linear differential equation 15 with the appropriate

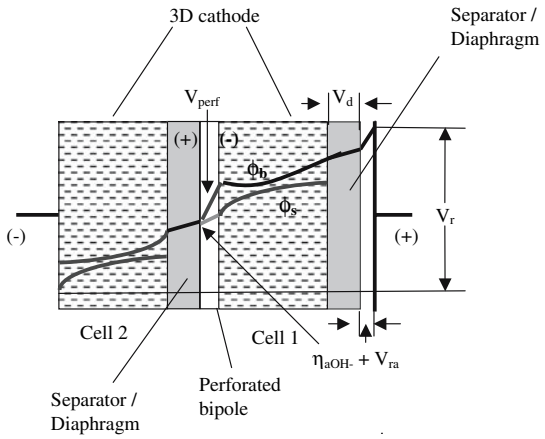

V_d	: Potential drop in the diaphragm	V
V_{perf}	: Potential drop in the perforation	V
V_r	: Reactor voltage	V
V_{ra}	: Equilibrium potential for hydroxyl oxidation at anode	V
η_{aOH^-}	: Overpotential for hydroxyl oxidation at anode	V
ϕ_b	: Electrolyte potential profile in 3D cathode	V
ϕ_s	: Electrode, potential profile in 3D cathode	V

Fig. 10 Voltage balance on a two-cell reactor

boundary conditions. Solution of this differential equation using Runge–Kutta requires a shooting type method (as all the boundary conditions are not at the initial value) and is further complicated by the presence of perforations that allow current bypass. This method of solution has problems in convergence and therefore an alternative method based on numerical solution of an electronic analogue [11] was developed in the present work.

3.2.1 *Modeling algorithm*

The methodology developed in this work involves breaking the total voltage balance into a combination of series and parallel resistances as shown in Fig. 11. The 3D cathode is broken into series and parallel circuits based on the effective electrode and electrolyte conductivity given by k_{aps} and k_{apb} respectively. At the anode of cell 1 the superficial current density (based on the cross-sectional area of the section Δz in Fig. 7) is j(1). The 3D cathode bed is divided into (n–1)/4 sections. Here n = 4m + 1 (m is an integer) is the number of current densities j(1), j(2)...j(n). The even current densities j(2), j(4)...j(n-1) in the 3D cathode are due to reaction (1) and the odd current densities j(3), j(5)...j(n) are due to reaction (2). By forming n independent equations one can solve for the n current densities j(1), j(2)...j(n). The n equations can be obtained by formulating the series and parallel resistances of Fig. 11 into n independent circuits. These independent circuits are solved using Kirchoff's law of currents. The n equations can then be solved for the unknown current densities j(1), j(2)...j(n) using Newton's method for the solution of nonlinear equations.

The two-cell reactor model can be used for a single-cell by setting the perforation coverage = 0.001 so as to make the current bypass insignificant in comparison to the Faradaic current.

First a model was developed to determine the peroxide current efficiency and specific energy on a two-cell reactor. The modeling scheme entailed considering a differential cross section of the reactor (cf. Fig. 7) and writing voltage, material, and energy balances for this differential volume.

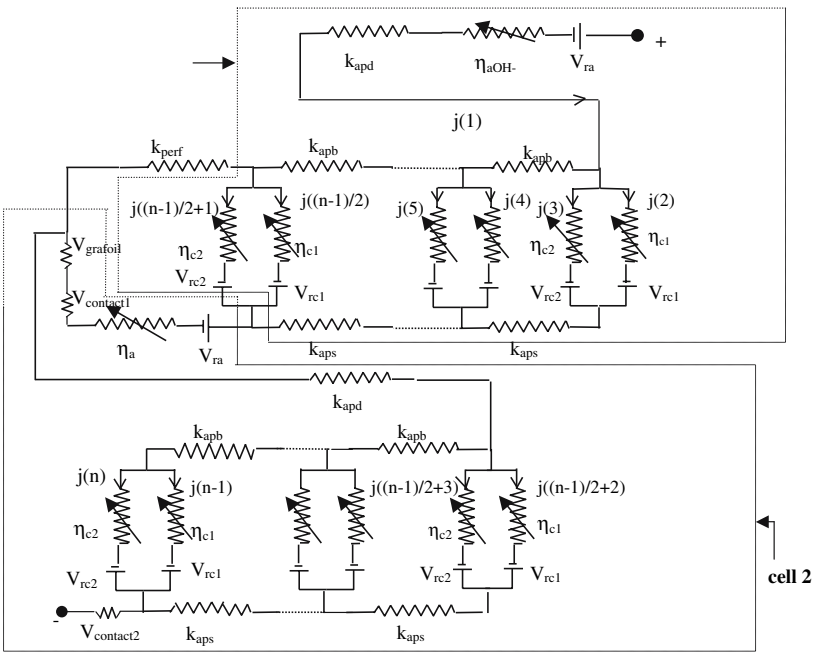

Fig. 11 Electronic analogue of voltage balance for one length increment on a two-cell reactor

j(1)	: Superficial current density	A m^{-2}
j(2),j(4)….j(n-1)	: Current densities for peroxide generation reaction (1) where n = 4m +1, m is an integer	A m^{-2}
j(3),j(5)…....j(n)	: Current densities for peroxide reduction reaction (2)	A m^{-2}
k_{apb}	: Effective electrolyte conductivity in cathode bed	S m^{-1}
k_{apd}	: Effective diaphragm conductivity	S m^{-1}
k_{perf}	: Effective electrolyte conductivity in perforation	S m^{-1}
k_{aps}	: Effective electrode conductivity of cathode bed	S m^{-1}
V_{ra}	: Equilibrium potential for hydroxyl oxidation at anode	V
V_{rc1}	: Equilibrium potential for perhydroxyl generation at cathode	V
V_{rc2}	: Equilibrium potential for perhydroxyl reduction at cathode	V
$V_{contact1}$	: Contact voltage drop between Grafoil and graphite on cell 1	V
$V_{contact2}$	: Contact voltage drop between Grafoil and graphite on cell 2	V
$V_{grafoil}$	: Voltage drop on Grafoil	V
η_{aOH-}	: Over potential for hydroxyl oxidation at anode	V
η_{c1}	: Over potential for perhydroxyl generation (1) at cathode	V
η_{c2}	: Over potential for perhydroxyl reduction (2) at cathode	V

The reactor was then integrated from the inlet (bottom) to the outlet (top) along the length of the reactor by forward differencing for *lin* length increments. The calculations for the two-cell model are described here.

Properties The relations used to calculate the material properties and fluid dynamic features in the reactor are summarized in Table 3. All symbols and units are as defined in the Nomenclature.

Current densities and potentials The relations used calculate current density and potential at the cathode and anode are summarized in the following Eqs. 16– 42.

The mass transfer limited real current density for reactions 1 and 2 on the cathode:

$$j_{lim1} = 2000F\ k_O C_{O_2} \tag{16}$$

Table 3 Properties and fluid dynamics

Quantity	Relation	Source
Partial pressure	$P_{H_2O} = e^{\left(16.5362 - \frac{3985.44}{T - 38.9974}\right)}$	[12, 13]
	$P_{O_2} = P - P_{H_2O}$	
Fluid density	$\rho_L = 1000(1 + 0.04C_{Na^+})$	
	$\rho_G = \frac{M_{O_2} P_{O_2}}{RT}$	[14]
Fluid viscosity	$\mu_L = 0.001(1 + 0.5C_{Na^+})10^{-10.73+1828/T+0.01966T-1.466\times10^{-5}T^2}$	[14]
	μ_G = 1e–6[18.11 + 0.6632 T–(1.879 × 10^{-4})T^2]	[14]
Species diffusivity	$D_{HO_2^-} = \frac{0.001 D^0_{HO_2^-} T}{298\,\mu_L}$	
	$D_{OH^-} = \frac{0.001 D^0_{OH^-} T}{298\,\mu_L}$	
	$D_{Na^+} = \frac{0.001 D^0_{Na^+} T}{298\,\mu_L}$	[14, 15]
	$D_{O_2} = \frac{0.001 D^0_{O_2} T}{298\,\mu_L}$	
Effective diffusivity	$D_{dHO_2^-} = \frac{2 D_{HO_2^-} \varepsilon_d}{3 - \varepsilon_d}$	
	$D_{dOH^-} = \frac{2 D_{OH^-} \varepsilon_d}{3 - \varepsilon_d}$	[16]
Oxygen solubility	$C_{O_2} = \frac{(P_{O_2}/101)}{H}$	
	$\log\left(\frac{C_{electrolyte,O_2}}{C_{H_2O,O_2}}\right) = \Sigma_j K_{s,j} C_{electrolyte(j)}$	
	$K_s = \Sigma_i (h_i + h_G) n_i$	[17, 18]
	$H = \frac{H_o}{(C_{NaOH,O_2}/C_{H_2O,O_2})}$	
	$H_O = e^{\left[\frac{0.046T^2 + 203.35T\ln(T/298) - (299.378 + 0.092T)(T-298) 20.591\times10^3}{8.3144T}\right]}$	[22]
Specific surface	$s = 4\frac{(1-\varepsilon_b)}{d_f}$	
Pressure gradient	$\nabla P_{LG} = \frac{\Delta P_{LG}}{\Delta Z} = \left(\frac{liq}{t_b w}\right)\left(0.36 + 1.182\left(\frac{g}{liq}\right)^{0.618}\right)^2$	[10]
Liquid hold-up	$h_l = 1 - 0.907(liq/(t_b\ w\ ))^{-0.362}(g/(t_b\ w\ ))^{0.301}$	[10]
Mass transfer	$k_O = 5.9\left(\frac{liq}{t_b w}\right)^{0.372}\left(\frac{g}{t_b w}\right)^{0.232}\left(\frac{1}{s}\right)$	[10]
	$k_{HO_2^-} = \frac{k_O D_{HO_2^-}}{D_{O_2}}$	
Conductivity	$k_{apl} = \left(0.0726 + 19.576C_{Na^+} - 3.035C^2_{Na^+}\right)(1 + 0.023(T - 293))$	[14]
	$k_{apd} = \frac{2k_{apl}\varepsilon_d}{(3-\varepsilon_d)}$	[15]
	$k_{apb} = \frac{2k_{apl}\varepsilon_b h_l}{(3-\varepsilon_b h_l)}$	[16]
	$k_{aps} = 10 + 2800\left(\frac{1-\varepsilon_b}{\varepsilon_o}\right)^{1.55}$	[16]
	$k_{perf} = k_{apl}$	[19]

$$j_{lim2} = 2000F\, k_{HO_2^-} C_{HO_2^-} \tag{17}$$

The total superficial current density on the anode (Fig. 11) is denoted by j(1). The real current densities on the cathode due to perhydroxyl ion formation and perhydroxyl ion reduction are denoted respectively as j(2), j(4), j(n–1) and j(3), j(5)...j(n). Note here n = 4m +1 where m is a positive integer.

Equilibrium potential for reactions (1), (2) and (4):

$$V_{rc1} = -0.076 - \left(\frac{RT}{2F}\right) \ln\left(\frac{C_{HO_2^-} C_{OH^-}}{P_{O_2}}\right) \tag{18}$$

$$V_{rc2} = 0.878 - \left(\frac{RT}{2F}\right) \ln\left(\frac{C_{OH^-}^3}{C_{HO_2^-}}\right) \tag{19}$$

$$V_{ra} = 0.401 - \left(\frac{RT}{4F}\right) \ln\left(\frac{C_{aOH^-}^4}{P_{O_2}}\right) \tag{20}$$

Reaction (4) is considered the primary anode reaction and all perhydroxyl ions reaching the anode are assumed oxidized by reaction (5). When carrying out voltage (a.k.a. charge), material and energy balances over the first differential section shown in Fig. 7, C_{aOH^-} is assumed to be equal to C_{OH^-}.

Over-potential on the anode due to reaction (4) is:

$$\eta_a = a_a + b_a \ln(j(1)) \tag{21}$$

where a_a and b_a are Tafel constants for reaction (4) on nickel:

$$a_a = \frac{-RT \ln(j_{0a})}{\alpha_a F} \tag{22}$$

$$b_a = \frac{RT}{\alpha_a F} \tag{23}$$

The oxidation of perhydroxyl ions on the anode is not considered in the voltage balance; however the perhydroxyl loss through the diaphragm is accounted for in the material balance.

Diaphragm potential drop:

$$V_d = \frac{j(1) t_d}{k_{apd}} \tag{24}$$

Over-potential due to perhydroxyl ion formation (1):

$$\eta_{c1} = a_{c1} + b_{c1} \ln(j(k)) - b_{c1} \ln\left(1 - \frac{j(k)}{j_{lim1}}\right) \tag{25}$$

where k = 2, 4... (n–1) and the Tafel parameters for reaction (1) and are:

$$a_{c1} = \frac{-RT \ln(j_{01})}{\alpha_1 F} \tag{26}$$

$$b_{c1} = \frac{RT}{\alpha_1 F} \tag{27}$$

Exchange current density for reaction (1) on graphite:

$$j_{01} = 2000 F k_1^0 \exp\left[\left(\frac{-E_{a1}}{R}\right)\left(\frac{1}{T} - \frac{1}{288}\right)\right] C_{O_2} \exp\left(\frac{-\alpha_1 F V_{rc1}}{RT}\right) \tag{28}$$

Over-potential due to perhydroxyl ion reduction (2):

$$\eta_{c2} = a_{c2} + b_{c2} \ln(j(k)) - b_{c2} \ln\left(1 - \frac{j(k)}{j_{lim2}}\right) \tag{29}$$

where k = 3,5...n and the Tafel parameters for reaction (2):

$$a_{c2} = \frac{-RT \ln(j_{02})}{\alpha_2 F} \tag{30}$$

$$b_{c2} = \frac{RT}{\alpha_2 F} \tag{31}$$

and the exchange current density for reaction (2) on graphite is:

$$j_{02} = 2000 F k_2^0 \exp\left[\left(\frac{-E_{a2}}{R}\right)\left(\frac{1}{T} - \frac{1}{288}\right)\right] C_{HO_2^-} \exp\left(\frac{-\alpha_2 F\ V_{rc2}}{RT}\right) \tag{32}$$

Using Eqs. 16–32 and Kirchoff's laws for currents the circuit in Fig. 11 is solved for currents j(1) to j(n) for the differential section shown in Fig. 7.

The superficial current density on the anode due to perhydroxyl ion oxidation (5) is the sum of diffusive, convective and migrative flux:

$$i_{1HO_2^-} = 1000\left[\frac{\left(D_{dHO_2^-} + D_{ed}\right)\left(C_{1HO_2^-} - 0\right)F}{t_d} + \frac{j(1) D_{dHO_2^-} F^2 C_{1HO_2^-}}{k_{apd} RT}\right] \tag{33}$$

$$i_{2HO_2^-} = 1000\left[\frac{\left(D_{dHO_2^-} + D_{ed}\right)\left(C_{2HO_2^-} - 0\right)F}{t_d} + \frac{j(1) D_{dHO_2^-} F^2 C_{2HO_2^-}}{k_{apd} RT}\right] \tag{34}$$

The convective flux may be accounted for by introducing an eddy diffusivity term D_{ed} in the diffusive

component of Eqs. 33 and 34. The superficial current densities due to hydroxyl ion oxidation (4) on the anode of cell 1 and 2 are given by:

$$i_{1OH^-} = j(1) - i_{1HO_2^-} \tag{35}$$

$$i_{2OH^-} = j(1) - i_{2HO_2^-} \tag{36}$$

Likewise, the superficial current density on the anode due to diffusive, convective and migrative flux of hydroxyl ions is:

$$i_{1OH^-} = 1000\left[\frac{\left(D_{dOH^-} + D_{ed}\right)\left(C_{OH^-} - C_{aOH^-}\right)F}{t_d} + \frac{D_{dOH^-}F^2\left(\left(C_{OH^-} + C_{aOH^-}\right)\right)j(1)}{2\ k_{apd}RT}\right] \tag{37}$$

Here C_{aOH^-} is the concentration of hydroxyl ions at the anode. This concentration was assumed to be equal to C_{OH^-} for the first differential section in Fig. 7. The subsequent values may be calculated by rearranging Eq. 37 in terms of C_{aOH^-}. In the migrative flux term of the hydroxyl ions, the concentration is averaged across the diaphragm, i.e. $(C_{OH^-} + C_{aOH^-})/2$.

Equation 37 can be rewritten for the hydroxyl ion concentration (C_{aOH^-}) at the anode:

$$C_{aOH^-} = \frac{\left(\frac{i_{1OH^-}}{1000} - \left(\frac{(D_{dOH^-}+D_{ed})F}{t_d} + \frac{D_{dOH^-}F^2 j(1)}{2k_{apd}RT}\right)C_{OH^-}\right)}{\left(\frac{D_{dOH^-}F^2 j(1)}{2k_{apd}RT} - \frac{(D_{dOH^-}+D_{ed})F}{t_d}\right)} \tag{38}$$

Since the hydroxyl concentration does not differ much for cells 1 and 2, therefore the C_{aOH^-} term is calculated from Eq. 38 for both the cells.

The total currents flowing through the cathode bed of cells 1 and 2 for reaction (1) are given by Eqs. 39 and 40, respectively, and for reaction (2) by (41) and (42), respectively:

$$\Sigma j_{1HO_2^-} = [j(2) + j(4) + \cdots j((n-1)/2)] \tag{39}$$

$$\Sigma j_{2HO_2^-} = [j((n-1)/2+2) + j((n-1)/2+4) + \cdots j(n-1)] \tag{40}$$

$$\Sigma j_{1OH^-} = [j(3) + j(5) + \cdots j((n-1)/2+1)] \tag{41}$$

$$\Sigma j_{2OH^-} = [j((n-1)/2+3) + j((n-1)/2+5) + \cdots j(n)] \tag{42}$$

Voltage (a.k.a. charge) balance There are n currents to be calculated in the circuit in Fig. 11 and these can be determined by solving n independent equations. The n independent non-linear equations were obtained by applying Kirchoff's laws for current and solved using Newton's method.

Material balance The concentrations of perhydroxyl at the exit of the differential section for cells 1 and 2 in Fig. 12 are given by:

The perhydroxyl ion concentration is then averaged using the following equation:

$$C^{new}_{1HO_2^-} = \left(C_{1HO_2^-} + \frac{w\Delta z\left(\left(\frac{st_b}{(n-1)/4}\right)\Sigma j_{1HO_2^-} - \left(\frac{st_b}{(n-1)/4}\right)\Sigma j_{1OH^-} - i_{1HO_2^-}\right)}{2F\ liq/\rho_L}\right) \tag{43}$$

$$C^{new}_{2HO_2^-} = \left(C_{2HO_2^-} + \frac{w\Delta z\left(\left(\frac{st_b}{(n-1)/4}\right)\Sigma j_{2HO_2^-} - \left(\frac{st_b}{(n-1)/4}\right)\Sigma j_{2OH^-} - i_{2HO_2^-}\right)}{2F\ liq/\rho_L}\right) \tag{44}$$

$$C^{new}_{HO_2^-} = \left(C^{new}_{1HO_2^-} + C^{new}_{2HO_2^-}\right)/2 \tag{45}$$

The concentrations of perhydroxyl at the exit of the differential section for cells 1 and 2 are:

The hydroxyl ion concentration is then averaged using the following equation:

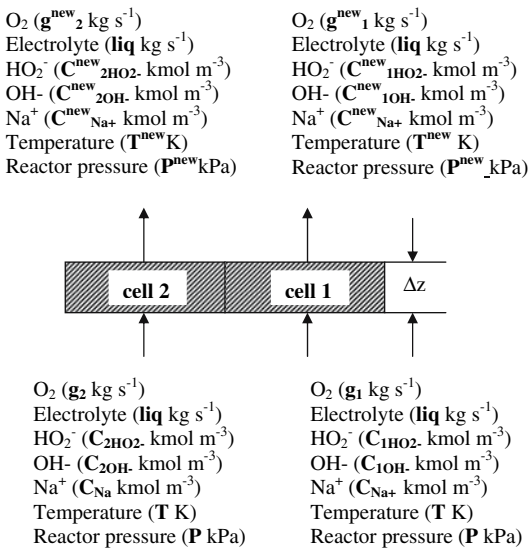

Fig. 12 Differential section of Figure 7

The O_2 generated in cell 2 is disengaged through the perforations and adds to the cell 1 flow rate. Accounting for this O_2 generation the O_2 flow rate in cell 1 is given by:

$$g_1^{new} = g_1 + \frac{M_{O_2}\left(\frac{i_{2HO_2^-}}{2} + \frac{i_{2OH^-}}{2} - \left(\frac{st_b}{(n-1)/4}\right)\Sigma j_{1HO_2^-}\right)w\Delta z}{2F} \tag{53}$$

$$g_2^{new} = g_2 - \frac{M_{O_2}\left(\left(\frac{st_b}{(n-1)/4}\right)\Sigma j_{2HO_2^-}\right)w\Delta z}{2F} \tag{54}$$

The flow rate of O_2 is averaged for each incremental height as follows:

$$g^{new} = \left(g_1^{new} + g_2^{new}\right)/2 \tag{55}$$

$$C_{1OH^-}^{new} = \left(C_{1OH^-} + \frac{w\Delta z\left(\left(\frac{st_b}{(n-1)/4}\right)\Sigma j_{1HO_2^-} + 3\left(\frac{st_b}{(n-1)/4}\right)\Sigma j_{1OH^-} - 2i_{1OH^-}\right)}{2F\ liq/\rho_L}\right) \tag{46}$$

$$C_{2OH^-}^{new} = \left(C_{2OH^-} + \frac{w\Delta z\left(\left(\frac{st_b}{(n-1)/4}\right)\Sigma j_{2HO_2^-} + 3\left(\frac{st_b}{(n-1)/4}\right)\Sigma j_{2OH^-} - 2i_{2OH^-}\right)}{2F\ liq/\rho_L}\right) \tag{47}$$

$$C_{OH^-}^{new} = \left(C_{1OH^-}^{new} + C_{2OH^-}^{new}\right)/2 \tag{48}$$

The sodium ion concentration does not change and is given by:

$$C_{Na^+}^{new} = C_{Na^+} \tag{49}$$

The concentrations of perhydroxyl, hydroxyl and sodium ions calculated in Eqs. 45, 48 and 49 are initialized again in the Eqs. 50–52, respectively, to allow voltage, material and energy balances over the next section of the reactor (Fig. 7), i.e.,

$$C_{HO_2^-} = C_{HO_2^-}^{new} \tag{50}$$

$$C_{OH^-} = C_{OH^-}^{new} \tag{51}$$

$$C_{Na^+} = C_{Na^+}^{new} \tag{52}$$

The oxygen flow exiting the differential section of Fig. 12 is calculated by subtracting the oxygen used in reaction (1).

The O_2 flow rate must be reinitialized in order to carry out the voltage, material and energy balances on the next section (Fig. 7) in the reactor, i.e.,

$$g = g^{new} \tag{56}$$

The oxygen generated on the anode of cell 1 is not accounted for in Eq. 54 as it flows through the dummy anode in Fig. 7 and does not contribute to any further reactions in the reactor.

The concentrations of perhydroxyl, hydroxyl and oxygen flow rate can be determined accounting for the consumption and generation of these species in the section Δz of Fig. 7.

Energy balance An energy balance on the section Δz of the reactor in Fig. 7 and gives:

$$\begin{aligned}&\text{heat input} + \text{heat generation} = \text{heat output}\\&\quad + \text{heat accumulation}\end{aligned} \tag{57}$$

At steady state the accumulation term is zero; therefore for 2 cells, and neglecting sensible heat in the gas:

$$\text{heat output} - \text{heat input} = \left[2(\text{liq})c_l(\Delta T) - \frac{1000\left(\frac{P_{H_2O}}{P - P_{H_2O}}\right)(2g)\Delta H_{evap}}{M_{O_2}}\right] = \text{heat generation} \quad (58)$$

where Δ T is the temperature change across the section Δ z in Fig. 7 and ΔHevap is the heat of vaporization of water (42.85 kJ/mol) [23].

Neglecting entropy effects, the heat generation is approximated by:

$$\text{heat generation} = 0.001(V_r + 2V_{rc1} - 2V_{ra})j(1)w\Delta z \quad (59)$$

Equating 58 with 59 yields

$$\Delta T = \frac{(0.001(V_r + 2V_{rc1} - 2V_{ra})j(1)w\Delta z)}{2(\text{liq})c_l} - \frac{1000\left(\frac{P_{H_2O}}{P - P_{H_2O}}\right)(g)\Delta H_{evap}}{M_{O_2}(\text{liq})c_l} \quad (60)$$

The water vapour pressure P_{H_2O} is a function of temperature of the reactor and is calculated at the local temperature prevailing in the reactor with the assumption that the temperature does not significantly differ in two length increments in Fig. 7. Sensible heat carried by O_2 is neglected as it contributes little to the overall energy balance.

Current efficiency and current bypass The current efficiency (C.E.) for perhydroxyl generation and the bypass current fraction (C.B.) are calculated from Eqs. 61 and 62.

$$\text{C.E.} = \frac{2000F\ C_{HO_2^-}(\text{liq}/\rho_L)}{I_{reactor}} \quad (61)$$

$$\text{C.B.} = \frac{I_{reactor} - w\ l_e\left(\Sigma_1^{lin}\Sigma j_{1HO_2^-} - \Sigma_1^{lin}\Sigma j_{1OH^-}\right)}{2I_{reactor}} \quad (62)$$

where $\Sigma_1^{lin}\Sigma j_{1HO_2^-}$ and $\Sigma_1^{lin}\Sigma j_{1OH^-}$ are the total currents for perhydroxyl generation and reduction respectively in cell 1 and are obtained using (39) and (41) and summing over the cell length.

Specific energy The specific electrochemical energy for perhydroxyl generation (S.E.) is:

$$\text{S.E.} = \frac{2FV_r}{2(3600)(34)\text{C.E.}} \quad (63)$$

The above equations were solved using a code based on an algorithm written in MATLAB.

3.2.2 Parameters in the model

The parameters used in modeling the two-cell reactor for peroxide generation are specified in Table 4. To achieve convergence of the calculations, the number length increments *lin* was selected as 100 and the number of circuits/equations n as 77. E.g. The effect of increasing number of circuits/equations n on superficial current density (kA m^{-2}) at 3.8 V for a two-cell reactor is shown in Fig. 13. This Figure shows that as the number of circuits increases, the superficial current density increases and stabilizes at a value of $\sim$3.8 kA m^{-2} for n > 25; therefore n = 77 is a good choice of the number of circuits/equations for the convergence of the electrochemical analogue circuit.

4 Results and discussion

Previous work [3] described the experimental scale-up of a perforated bipole trickle bed electrochemical reactor from a superficial cathode area per cell of 3×10^{-3} (reactor-A) to 25×10^{-3} m^2 (reactor-B) In that work the peroxide current efficiency was increased by changing the diaphragm separator material from porous polypropylene (SCIMAT 700/20 from SCIMAT, New Jersey, USA) to microporous-polyethylene (SOLUPOR EH-06A from DSM Solutech, Heerlens, Netherlands). That result implied that the polyethylene diaphragm increased the peroxide current efficiency relative to the polypropylene diaphragm by lowering convective loss of peroxide to the anode.

Figures 14 and 15, Table 5 compare the experimental values of performance indicators with each diaphragm in a single-cell reactor-B, against the corresponding modeled results with 2 M NaOH and an assumed eddy diffusion coefficient (D_{ed}) of zero. The agreement here between the experimental and modeled current efficiencies with the polyethylene diaphragm indicates that this separator effectively constrains peroxide convection to the anode. A similar agreement can be obtained for the polypropylene diaphragm by increasing D_{ed} to 2×10^{-8} m^2 s^{-1}. These results show that the model can predict the experimental peroxide concentration and current efficiency using D_{ed} as a single fitting parameter.

The experimental specific energies for peroxide generation for the polyethylene diaphragm were lower than that for the polypropylene diaphragm as a result of the higher current efficiencies. However, the modeled specific energy values are all lower than the experimental values. A plausible reason for the low specific energies predicted by the model may be that the blocking effect of oxygen gas on the anode was not included in the model. The rate of oxygen generation at the anode is proportional to the superficial current density and (at steady-state) must be

Table 4 Parameters in the model

Parameter	Meaning	Source	Value	Units
c_l	Electrolyte heat capacity	[12] Averaged (298–353 K)	4	kJ $kg^{-1}K^{-1}$
c_g	Gas (O_2) heat capacity	[14] Averaged (298–353 K)	0.9	kJ $kg^{-1}K^{-1}$
$C_{HO_2^-}$	Perhydroxyl ion concentration	Measured	1×10^{-6} (reactor inlet)*	kmol m^{-3}
C_{OH^-}	Hydroxyl concentration	Measured	2 (reactor inlet)	kmol m^{-3}
C_{Na^+}	Sodium ion concentration	Measured	2	kmol m^{-3}
D_{ed}	Eddy diffusivity through the diaphragm	to fit the experimental curve	0– 2×10^{-8}	m^2s^{-1}
$D^0_{HO_2^-}$	Diffusivity of perhydroxyl ion at infinite dilution	[14] at 298 K	1.5×10^{-9}	m^2s^{-1}
$D^0_{OH^-}$	Diffusivity of hydroxyl ion at infinite dilution	[14] at 298 K	5.3×10^{-9}	m^2s^{-1}
$D^0_{Na^+}$	Diffusivity of sodium at infinite dilution	[14] at 298 K	1.3×10^{-9}	m^2s^{-1}
$D^0_{O_2}$	Diffusivity of oxygen at infinite dilution	[14] at 298 K	2.4×10^{-9}	$m^2 s^{-1}$
g	Gas flow rate per cell	Measured	1.7×10^{-5}	kg s^{-1}
liq	Liquid flow rate per cell	Measured	6.7×10^{-4}	kg s^{-1}
d_f	Graphite felt fibre diameter	Metaullics systems Inc.	2×10^{-5}	m
ε_b	Graphite felt porosity after compression	[19]	0.87	dimensionless
ε_d	Diaphragm porosity	SCIMAT 700/20	0.80	dimensionless
		SOLUPOR E075-9H06A	0.76	
ε_o	Graphite porosity felt before compression	Metaullics systems Inc.	0.95	dimensionless
k_1^0	Rate constant for reaction (1)	[20] at 288 K	5×10^{-7}	m s^{-1}
k_2^0	Rate constant for reaction (2)	[20] at 288 K	1.6×10^{-9}	m s^{-1}
α_1	Charge transfer coefficient for single step of reaction (1)	[20] at 288 K	0.543	dimensionless
α_2	Charge transfer coefficient for single step of reaction (2)	[20] at 288 K	0.263	dimensionless
E_{a1}	Activation energy for reaction (1) on carbon	[21]	25530	J mol^{-1}
E_{a2}	Activation energy for reaction (2) on carbon	[21]	25530	J mol^{-1}
t_b	Thickness of graphite felt (compressed)	Measured	3.2×10^{-3}	m
t_d	Thickness of diaphragm	SCIMAT 700/20	120×10^{-6}	m
		SOLUPOR E075-9H06A	39×10^{-6}	
t_o	Thickness of graphite felt (un -Compressed)	As received	8.2×10^{-3}	m
l_e	Length of the reactor	Measured	0.63	m
w	Width of the reactor	Measured	0.04	m
T	Reactor temperature	Measured	293 (reactor inlet)	K
P	Reactor pressure	Measured	700–900 (reactor inlet)	kPa (abs.)
V_r	Reactor voltage	Measured	1.5–6.5	V
j_{0a}	Exchange current density for reaction (4) on nickel anode	[21] at 296 K assumed constant for entire reactor	1.1×10^{-7}	A m^{-2}
b_a	Tafel slope for reaction (4) on the anode	[21] at 296 K assumed constant for entire reactor	0.043	V $decade^{-1}$
$k_{contact}$	Area conductivity between Grafoil and graphite felt	Measured	5000	S m^{-2}
$k_{grafoil}$	Conductivity of Grafoil	Measured	1×10^4	S m^{-1}

Table 4 continued

Parameter	Meaning	Source	Value	Units
perf	Fraction perforation area in the bipole	Measured	0.02	dimensionless
n	Circuits solved (Fig. 11)	Convergence criterion	77	dimensionless
lin	Number of length increments in Fig. 9	Convergence criterion	100	dimensionless

** The inlet concentration of perhydroxyl ions is kept as 1×10^{-6} kmol m^{-3} to avoid convergence close-up problems in modeling

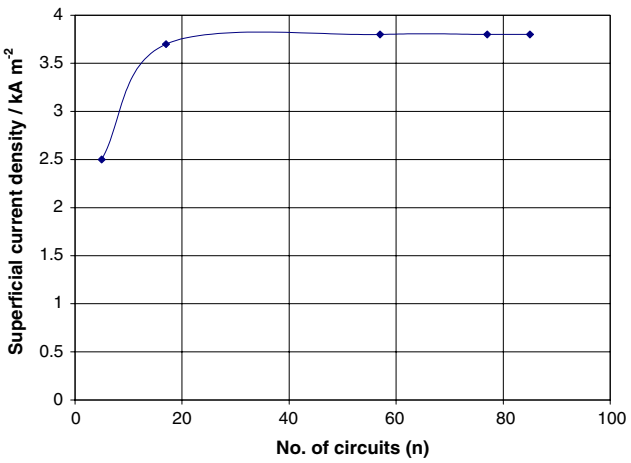

Fig. 13 Effect of number of circuits on the superficial current density

matched by the rate of oxygen disengagement from the anode to the adjacent electrode. Increasing current density raises the gas hold-up in the nickel mesh anode and lowers its effective area, thus inflating the cell voltage and specific energy. This gas hold-up/wetting effect is corroborated by the corrosion of the anode (nickel mesh) at current densities above about 3 kA m^{-2}. The choice of anode material/surface area is critical to the efficient disengagement of oxygen and may ultimately be the key to a commercial electrochemical route for peroxide generation.

Figures 16 and 17 compare the experimental values of performance indicators with each diaphragm in a two-cell reactor-B, against the corresponding modeled results with 2 M NaOH, 2% bipole perforation coverage and $D_{ed} = 0$. As for a single-cell reactor the experimental peroxide concentration and current efficiency with the polyethylene diaphragm are higher than those with the polypropylene diaphragm and are predicted with D_{ed} set at zero.

Also the specific energy values for peroxide generation in the two-cell reactor with employing the polyethylene diaphragm are closer to the modeled values than in the case of the single cell. This result may be due to more facile disengagement of oxygen from the anodes of a multi-cell reactor and indicates good prospects for reactor scale-up, provided the issue of fluid distribution between cells can be resolved [3].

Both the single- and two-cell reactor models calculate values for peroxide concentration and current efficiency that are close to the experimental values. This model could be used in future work on peroxide generation, particularly to scale-up the perforated bipole reactor to more than two cells—as would be needed for an industrial process. The novel way of modeling the bipolar electrochemical reactor described in this work may be employed for other reactors with 3D electrodes.

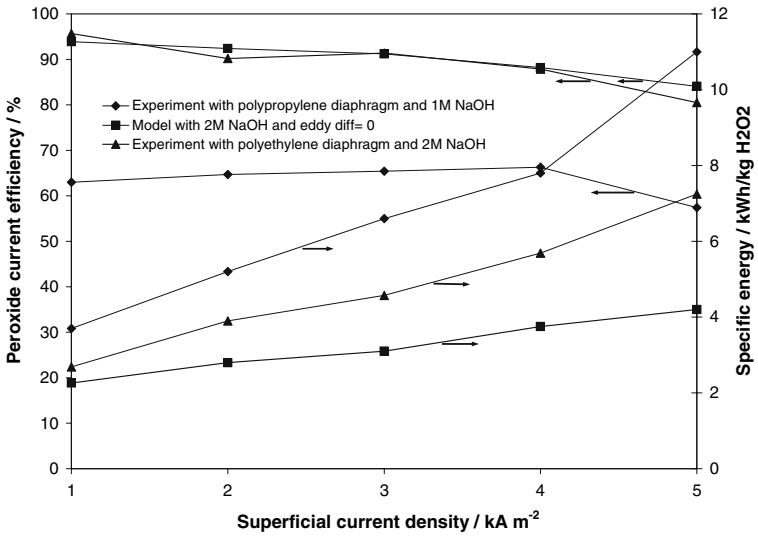

Fig. 14 Peroxide current efficiency and specific energy for peroxide generation versus superficial current density for a single-cell reactor-B for modeled and experimental runs (other conditions as in Table 5)

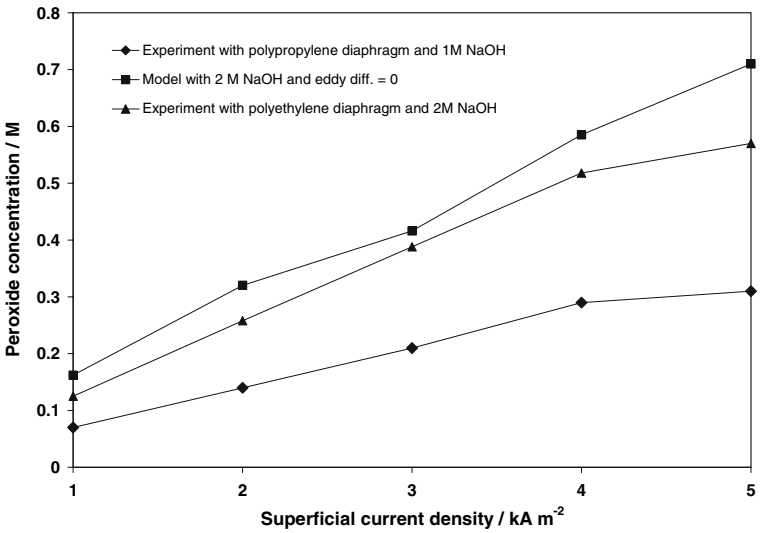

Fig. 15 Peroxide concentration versus superficial current density for a single-cell reactor-B for modeled and experimental runs (other conditions as in Table 5)

Table 5 Experimental conditions

Experiment →		Figs. 14, 15	Figs. 16, 17
NaOH conc.	M	1.0/2.0	1.0/2.0
NaOH flow	ml/min	40–50	75–95
O_2 flow	ml STP/min/cell	400–600	400–600
Reactor pressure	kPa(abs) in–out	700–500	700–500
Reactor	°C in–out	20–80 °C	20–80 °C
Anode/bipole		Ni 100#/Grafoil	Ni 100#/Grafoil
Bipole perforation	diam mm/coverage %	1.6/2	1.6/2
Diaphragm type		SCIMAT 700/20 SOLUPOREH-06A	SCIMAT 700/20 SOLUPOREH-06A
Cathode	Thickness mm/porosity %	Graphite felt 3.2/87	Graphite felt 3.2/87
No. of cells		1	2

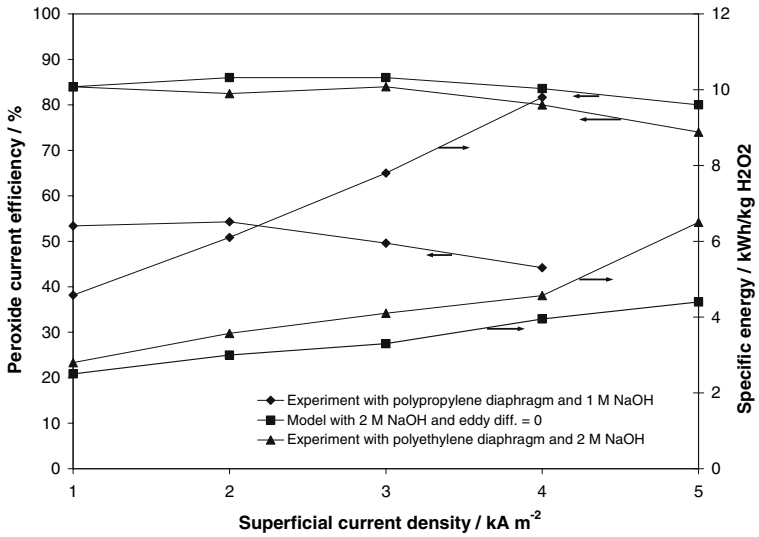

Fig. 16 Peroxide current efficiency and specific energy for peroxide generation versus superficial current density for the two-cell reactor-B for modeled and experimental runs (other conditions as Table 5)

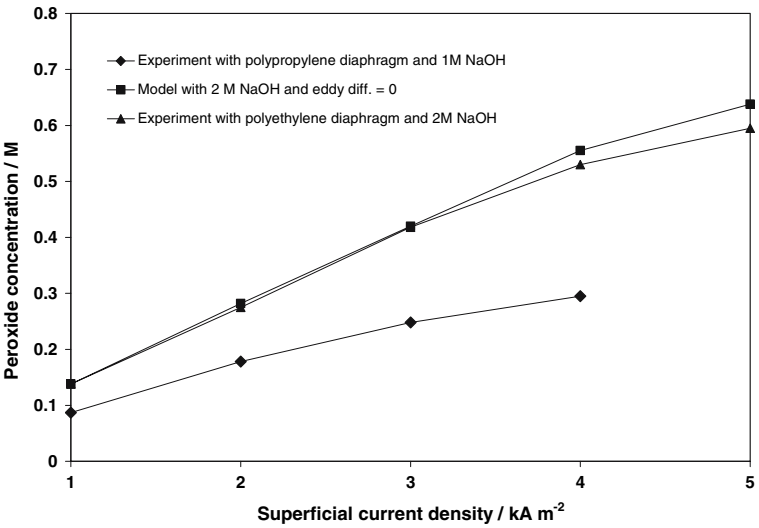

Fig. 17 Peroxide concentration versus superficial current density for the two-cell reactor-B for modeled and experimental runs (other conditions as in Table 5)

5 Conclusions

A method has been developed to model the perforated bipole trickle-bed electrochemical reactor. This model has novelty in terms of treating the flow-by 3D electrode as an electronic analogue circuit that allows algebraic calculation the potential distribution in the matrix and accounts for ionic current bypass losses through the bipole perforations, together with composition, pressure and temperature gradients along the reactor length.

Using eddy diffusivity in the separator as the single adjustable variable the model gives a reasonably accurate prediction of the product peroxide concentration and current efficiency for superficial current densities up to 5 kA m^{-2} in both one and two-cell versions of reactor-B, but underestimates the electrochemical specific energy consumption by up to about 50 % (i.e. by 2–3 kWh/kg H_2O_2 at 5 kA m^{-2}). The low predicted values of specific energy are probably due to neglect of the blocking effect of oxygen gas in the anode matrix.

Backed by further experimental work this model may be developed to aid the design of multi-cell bipolar peroxide reactors and other electrochemical systems, in which 3D electrodes are employed in similar ways.

Acknowledgements This work was supported by grants from the Government of Canada through the Natural Science and Engineering Research Council (NSERC) and the "Wood Pulps" Network of Centre of Excellence, with facilities supplied by the University of British Columbia (U.B.C.) and the U.B.C. Pulp and Paper Centre.

References

1. Gupta N (2004) Scale-up of the perforated bipole trickle bed electrochemical reactor for the generation of alkaline peroxide,

PhD Thesis, University of British Columbia, Vancouver, BC, Canada
2. Gupta N, Oloman CW (2006) J Appl Electrochem 36:255
3. Gupta N, Oloman CW (2006) J Appl Electrochem 36:1133
4. Oloman C (1979) J Electrochem Soc 126:1885
5. Spalek O (1986) Coll Czech Chem Comm 51:1883
6. Sudoh M, Yamamoto M, Kawamoto T, Okajima K, Yamada N (1999) Electrochem Soc Proceedings, Electrochem Soc, New Jersey 99–39:207
7. Erdey L, Inczedy J (1955) Magyar Tudomanyos Akad Kem Todomanyok Osztalyanak Kozlemenyei 5:513
8. Enestova LS, Skurlatov LS, Fursina LA (1985) Zhurnal Fizicheskoi Khimii 58(4):914 (Russian)
9. Levenspiel O (1972) Chemical reaction engineering. John Wiley & Sons, New York
10. Hodgson I, Oloman C (1999) Chem Eng Sci 54(23):5777
11. Newman JS (2004) Electrochemical systems. Prentice Hall, New Jersey
12. Hooker (1977) Caustic soda product information manual. Hooker Chemical Company
13. Reklaitis GV (1983) Introduction to material and energy balances. John Wiley, NY
14. Lide D (ed) (1986) CRC Handbook of chemistry and physics 66th Ed. CRC Press Inc., Boca Raton, p 14
15. Oloman C (1996) Electrochemical processing for the pulp and paper industry. The Electrochemistry Consultancy, Romsey, UK
16. Neale GH, Nader WK (1973) AIChE J 19(1):112
17. Treybal M (1993) Mass transfer operations. McGraw Hill, Singapore
18. Hermann C, Dewes I, Schumpe A (1995) Chem Eng Sci 50:1673
19. Oloman C, Matte M, Lum C (1991) J Electrochem Soc 138(8):2330
20. Sudoh M, Kitaguchi H, Koide K (1985) J Chem Eng Jpn 18(4):364
21. Kinoshita K (1992) Electrochemical oxygen technology. John Wiley, NY
22. Tromans D (1998) Hydrometallurgy 48(3):327
23. Atkins PW (1978) Physical chemistry. Freeman & Company, San Francisco